Shock Waves (1999) 9: 367–379

Shock Waves

Numerical investigation of axisymmetric shock wave focusing over paraboloidal reflectors

S.M. Liang[1], L.N. Wu[2], R.L. Hsu[1]

[1] Institute of Aeronautics and Astronautics, National Cheng Kung University, Tainan, Taiwan, Republic of China
[2] Air Asia Company, Tainan, Taiwan, Republic of China

Received 13 January 1998 / Accepted 10 November 1998

Abstract. The problem of a plane shock wave incident to a paraboloidal reflector is numerically investigated. The numerical solver used is developed by an improved, implicit, upwind total variation diminishing scheme in a finite-volume approach. The real-gas effect is taken into account if high temperature occurs. The solver is validated on four test problems. The complicated flow fields of axisymmetric shock wave focusing for different-depth reflectors at various incident shock Mach numbers are studied. An interesting result of a maximum pressure happening at the reflector center is found. This is due to the occurrence of an implosion phenomenon. A maximum temperature might occur at the reflector center or at other locations, depending on the incident shock Mach number and the reflector depth. Moreover, vortical flows induced by shock wave focusing and their formation mechanism are explored. It was found that the vortices near the reflector are caused by a ring-shaped shock/slipline interaction. Owing to the slipline on the symmetry axis, a jet flow is induced, resulting in the formation of vortices near the symmetry axis.

Key words: Shock wave focusing, Real-gas effects, Implosion phenomenon, Sliplines

1 Introduction

Shock wave focusing in a medium such as air or water is a special flow behavior of rapid energy concentration at a small region, resulting in a high pressure at the focal region. The focal point, where a maximum pressure occurred, is referred to as a gasdynamic focus. The gasdynamic focus may be different from the geometric focus of a reflector due to the nonlinearity of shock wave focusing. Underwater shock wave focusing was successfully applied to lithotriptors for clinical treatment of human calculi, and shock wave focusing in air has applications in material science and nuclear engineering.

In this study, axisymmetric shock wave focusing in air is considered, since past literature that reporting on the complicated flow field of shock wave focusing is limited. The problem of interest is a plane shock wave which is incident on a paraboloidal reflector. In the past twenty years, there were many papers that related to the problem of shock wave focusing. No attempt is made to review all papers. Only some recent papers on shock wave focusing in a gas are mentioned here. Holl et al. (1991) used a modified Chester-Chisnell-Whitham (CCW) model to investigate the problem of reflected blast wave focusing, and showed that the CCW method is an economic tool for the analysis of shock focusing process. Izumi et al. (1991) experimentally and numerically studied focusing process of shock waves reflected from parabolic reflectors and its mechanism. In addition to the maximum pressure caused by shock wave focusing, Kishige et al. (1991) experimentally confirmed the existence of a high temperature caused by a focused shock wave in argon by radiation measurements. Apazidis (1994) theoretically studied weak shock focusing in a spherical region in confined three-dimensional axisymmetric chambers. He found that the pressure distribution on a converging spherical shock wave is not homogeneous. Liang et al. (1995) numerically investigated the detailed flow field of shock wave focusing over parabolic reflectors using the Euler solver. Inoue et al. (1995) computationally studied shock wave focusing in a log-spiral duct. They analyzed the detailed flow field of an imploding shock wave.

The mechanism of axisymmetric shock wave focusing over paraboloidal reflectors is basically the same as in a two-dimensional case. However, for an axisymmetric case, reflected shock waves coming from all directions, the pressure enhancement at the gasdynamic focus would be much greater than that for the corresponding two-dimensional case. The pressure enhancement is mainly dependent upon the incident shock Mach number and the reflector depth. Both the reflector shape and the incident shock Mach number also have an effect on the type of shock wave re-

---

Correspondence to: S.M. Liang

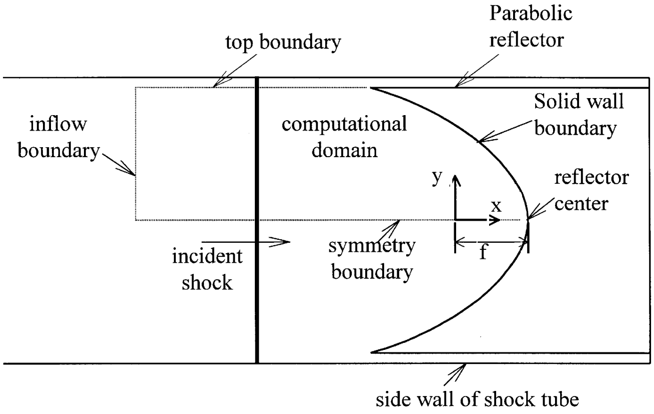

Fig. 1. A sketch of the shock wave focusing problem and computational domain

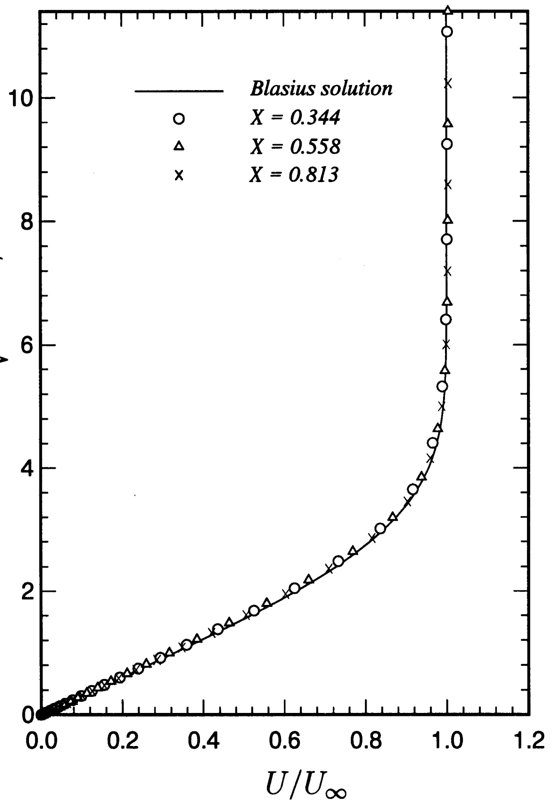

Fig. 2. Comparison of computed boundary layer profiles with the Blasius solution for a flat-plate problem, $M_S = 0.5, Re = 1 \times 10^4$

flection. The classification of the type of shock wave reflection from a wedge was done in detail by Ben-Dor (1992). Loosely speaking, there are two typical configurations of shock wave reflection. One is the type of regular reflection which consists of a reflected wave and an incident wave with an intersection at the reflection point. The other is the type of simple Mach reflection. A simple Mach reflection consists of a reflected wave, a slip line, a Mach stem and an incident wave with an intersection point, referred as a triple point.

For the development of a numerical solver, we employed the implicit total variation diminishing (TVD) method of Yee and Harten (1987) for shock capturing with the improved flux limiters of Liang et al. (1996) for scheme efficiency. Since a high temperature caused by shock wave focusing may occur, a real-gas effect is taken into account by using the curve fitting method of Srinivasan et al. (1987) for determining the value of the specific heat ratio. Thus our objective is to explore, with the numerical solver, flow fields such as a jet flow or an implosion phenomenon caused by shock wave reflection and focusing at different flow conditions, and to understand the formation mechanism of the jet flow and implosion phenomenon.

2 Mathematical formulation and numerical method

2.1 2D/axisymmetric governing equations

Neglecting the effects of external forces and heat transfer, the equations governing the flow are the continuity, momentum, and energy equations. In Cartesian coordinates, (x, y), the dimensionless equations can be expressed in a conservative form as

$$\begin{aligned} Q_t + (F - F_v/Re)_x + (G - G_v/Re)_y \\ + \alpha(H - H_v) = 0 \end{aligned} \quad (1)$$

where subscripts t, x, y denote partial derivatives and subscript v denotes the viscous terms. Equation (1) represents a planar flow for $\alpha = 0$, and $\alpha = 1$ for an axisymmetric flow. Q is the conservative variables, F, G, H the inviscid flux vectors, F_v, G_v, H_v the viscous flux vectors, and Re the Reynolds number, defined as $Re = \bar{\rho}_2 \bar{c}_2 \bar{l} / \bar{\mu}_2$. Note that the "bar" denotes dimensional quantities, ρ the density, c the speed of sound, μ the molecular viscosity, and $\bar{l}$ the characteristic length, defined as the focal length of the reflector. The subscript 2 denotes the flow condition behind the incident shock wave.

2.2 Real-gas effects

Since high temperatures can affect the value of the specific heat ratio, γ, the real-gas effect is taken into account when high temperature occurs. To determine the value of γ, the curve fitting method of Srinivasan et al. (1989) is used to compute the thermodynamic properties of air with the pressure and the density as two independent variables. Once the enthalpy, h, is determined, the value of γ is computed by the relation: $h\rho/p = \gamma/(\gamma - 1)$. Then the equivalent γ concept of Grossman and Walters (1989) for real gases is adopted.

2.3 Numerical method

For simple treatments of boundary conditions, Eq. (1) is transformed to a body-fitted coordinate, (ξ, η). Thus we have

$$\widehat{Q}_t + \left(\widehat{F} - \widehat{F}_v\right)_\xi + \left(\widehat{G} - \widehat{G}_v\right)_\eta + \alpha\left(\widehat{H} - \widehat{H}_v\right) = 0 \; , \quad (2)$$

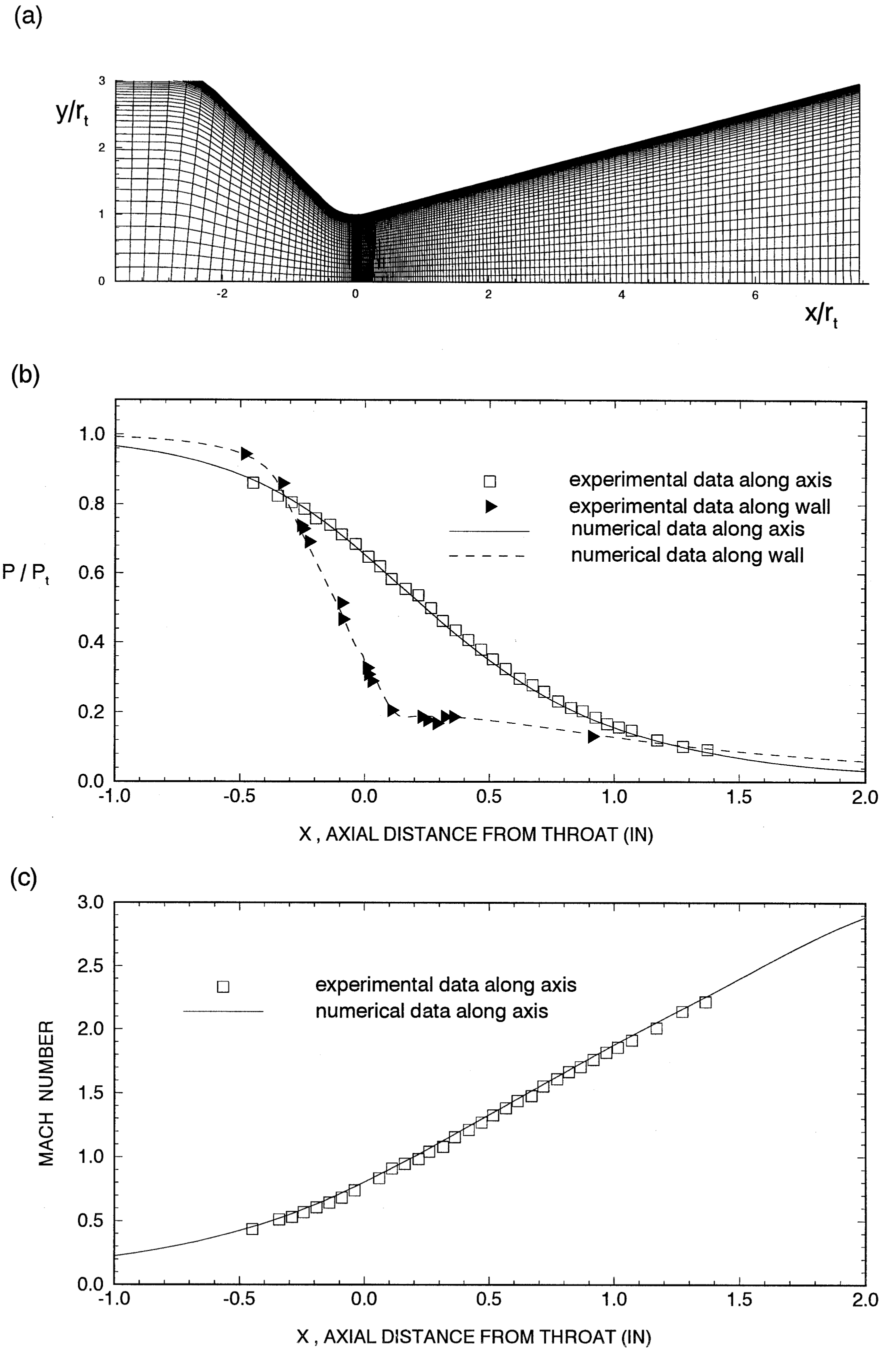

Fig. 3a–c. Comparison of the present result with the experimental data of Back et al. for a conical nozzle flow. **a** A 170 × 40 grid; **b** pressure distributions along the symmetry axis and the wall; **c** Mach number distribution along the symmetry axis

where $\widehat{Q}/J, \widehat{F} = (\xi_x F + \xi_y G)/J, \widehat{G} = (\eta_x F + \eta_y G)/J$, and J is the Jacobian defined as $J = (x_\xi y_\eta - x_\eta y_\xi)^{-1}$. Let $t = n\Delta t$, where Δt is the time step. For time integration, a trapezoidal method of second order is used. We get

$$R\left(\widehat{Q}^{n+1}\right) \equiv \widehat{Q}^{n+1} - \widehat{Q}^{n} + \frac{\Delta t}{2}\left\{FD|^{n} + FD|^{n+1}\right\} = 0 .$$

Here

$$FD = \left[\left(\widehat{F} - \widehat{F}_v\right)_\xi + \left(\widehat{G} - \widehat{G}_v\right)_\eta + \alpha\left(\widehat{H} - \widehat{H}_v\right)\right] .$$

For each time step, the Newton iteration is applied to improve time accuracy. With the replacement of the time index $n+1$ by S, we have

$$\frac{\mathrm{d}R\left(\widehat{Q}^{S}\right)}{\mathrm{d}\widehat{Q}^{S}}\left(\widehat{Q}^{S+1} - \widehat{Q}^{S}\right) = -R(\widehat{Q}^{S}) , \qquad (3)$$

where

$$\frac{\mathrm{d}R\left(\widehat{Q}^{S}\right)}{\mathrm{d}\widehat{Q}^{S}} = I + \frac{\Delta t}{2}\left[\left(\widehat{A} - \widehat{A}_v\right)_\xi + \left(\widehat{B} - \widehat{B}_v\right)_\eta + \alpha\left(\widehat{C} - \widehat{C}_v\right)\right]^{S} .$$

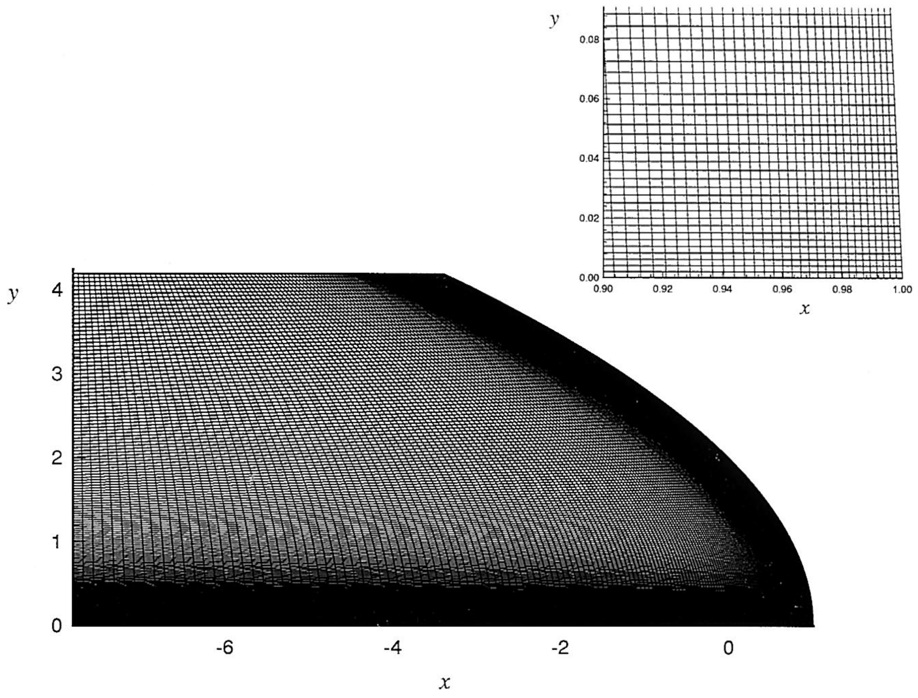

Fig. 4. A 200 × 200 grid for the 2D parabolic reflector and a grid subplot near the reflector center

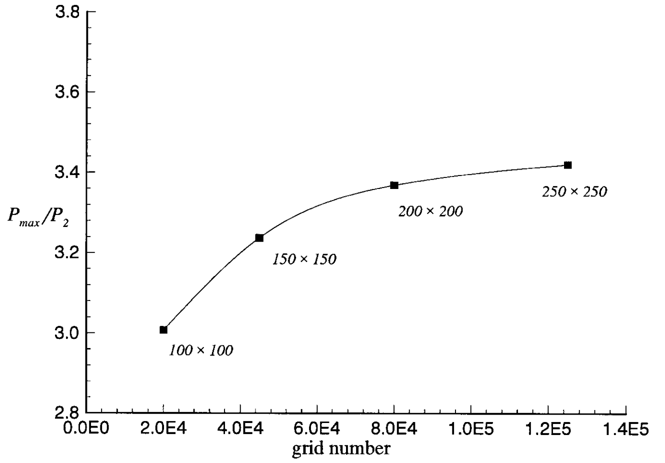

Fig. 5. The effect of grid number on the maximum pressure ratio for the 2D parabolic reflector, $M_S = 1.2$

Note that I denotes the identity matrix, and the flux Jacobian matrices are $\widehat{A} = \partial\widehat{F}/\partial\widehat{Q}$, $\widehat{A}_v = \partial\widehat{F}_v/\partial\widehat{Q}$, $\widehat{B} = \partial\widehat{G}/\partial\widehat{Q}$, $\widehat{B}_v = \partial\widehat{G}_v/\partial\widehat{Q}$, $\widehat{C} = \partial\widehat{H}/\partial\widehat{Q}$, $\widehat{C}_v = \partial\widehat{H}_v/\partial\widehat{Q}$.

For spatial discretization, a finite volume approach is employed. So we have a discretized equation of the form:

$$\left\{I + \frac{\Delta t}{2}\left[\Delta_\xi\left(\widehat{A} - \widehat{A}_v\right) + \Delta_\eta\left(\widehat{B} - \widehat{B}_v\right) + \alpha\left(\widehat{C} - \widehat{C}_v\right)\right]^S\right\}\left(\widehat{Q}^{S+1} - \widehat{Q}^S\right) = -\left(\widehat{Q}^S - \widehat{Q}^n\right) - \frac{1}{2}\left[(RHS)^n + (RHS)^S\right] , \quad (4)$$

where

$$RHS = \Delta t\left[\Delta_\xi\left(\widehat{F} - \widehat{F}_v\right) + \Delta_\eta\left(\widehat{G} - \widehat{G}_v\right) + \alpha\left(\widehat{H} - \widehat{H}_v\right)\right]$$

and $\Delta_\xi\widehat{F}_{j,k} = \tilde{F}_{j+1/2,k} - \tilde{F}_{j-1/2,k}, \Delta_\eta\widehat{G}_{j,k} = \tilde{G}_{j,k+1/2} - \tilde{F}_{j,k-1/2}$. The subscripts j, k are the grid indices along the ξ, η directions, respectively, and notations $\tilde{F}_{j\pm1/2}, \tilde{G}_{j,k\pm1/2}$ denote the numerical fluxes at the cell interfaces evaluated with Roe's averaging (1981). The constructions of $\Delta_\xi F_v$ and $\Delta_\eta G_v$ are based on central differences. The time step, Δt, is chosen to be the minimum of the local time steps over the computational domain:

$$\Delta t = \min_{j,k}\{\Delta t(\xi, \eta)\} , \quad \text{for all } \ j, k ,$$

where $\Delta t(\xi, \eta) = CFL \cdot \min(\Delta t_\xi, \Delta t_\eta)$, and CFL is the Courant number. In this study, CFL is set to be 1.5. Now we use the upwind TVD non-MUSCL scheme of Yee and Harten (1987). The operators $\widehat{A}, \widehat{B}$ are modified into H^ξ, H^η, respectively, in which a dissipation with improved flux limiters of Liang et al. (1996) is added. The details of H^ξ, H^η are omitted here. For more details, readers can refer to the paper by Yee and Harten. The improved flux limiters can enhance scheme efficency. Finally, the left-hand side of (4) is approximately factorized into a delta form for computational efficiency:

$$\left\{I + \frac{\Delta t}{2}\left[\left(H^\xi_{j+1/2,k} - H^\xi_{j-1/2,k}\right) - \left(\widehat{A}^{(v)}_{j+1/2,k} - \widehat{A}^{(v)}_{j-1/2,k}\right)\right]^S\right\}\Delta\widehat{Q}^* = -\left(\widehat{Q}^S - \widehat{Q}^n\right) - \frac{1}{2}[RHS]^n - \frac{1}{2}[RHS]^S \quad (5a)$$

$$\left\{I + \frac{\Delta t}{2}\left[\left(H^\eta_{j,k+1/2} - H^\eta_{j,k-1/2}\right) - \left(\widehat{B}^{(v)}_{j,k+1/2} - \widehat{B}^{(v)}_{j,k-1/2}\right) + \alpha\left(\widehat{C} - \widehat{C}_v\right)\right]^S\right\}\Delta\widehat{Q}^S = \Delta\widehat{Q}^* \quad (5b)$$

where $\Delta\widehat{Q}^* = \widehat{Q}^{S+1} - \widehat{Q}^S$. Equation (5) is iterated until convergence is satisfied for some integer m. The convergence criterion is set to be the l_2 norm of the density errors is less than 10^{-6}. The converged solution at time step $n+1$ is obtained, namely, $\widehat{Q}^{n+1} = \widehat{Q}^n + \Delta\widehat{Q}^m$.

2.4 Initial and boundary conditions

An incident shock wave with Mach number M_S is initially located at a distance away from the reflector. The initial thermodynamic properties prescribed ahead of and behind the shock are related by the Rankine-Hugoniot equations. As shown in Fig. 1, the boundary condition on the reflector surface is the no-slip condition. At the inflow boundary, the flow properties before the arrival of the reflected shock wave are fixed to be the flow condition behind the incident shock wave. Thus computation was terminated before the reflected shock wave crossing over the inflow boundary. The characteristic boundary condition is specified on the top boundary of the computational domain. On the symmetry axis, a second-order extrapolation of Harten and Osher (1987) is applied.

3 Results and discussion

3.1 Code validation

Case 1: The shock tube problem with high-temperature effects. A shock tube problem studied by Grossman and Walters (1989) was considered, and the result obtained is given in the paper by Liang et al. (1995). It was found that the Euler solver is able to accurately simulate the flow with high-temperature effects.

Case 2: Laminar boundary layer over a flat plate. A subsonic flow past a flat plate is calculated. The free stream condition is chosen to be $M_\infty = 0.5$, and the Reynolds number is $Re = 1 \times 10^4$. The computational domain is selected to be $\{(x, y), -0.25 \le x \le 1, 0 \le y \le 0.5\}$. The leading edge of the flat plate was located at $x = 0$. The coordinates and flow variables were nondimensionalized using the length of the flat plate and the free stream condition. At the inflow and top boundaries, the flow quantities are fixed at the free stream condition. At the outflow boundary, flow quantities are linearly extrapolated from the interior points. A uniform flow is chosen as an initial guess for numerical iteration. A grid with 31 × 41 grid points was used. The grid is uniformly distributed in the x direction and stretched exponentially upward from the wall, and the smallest grid size near the wall is 0.001. Numerical iteration is terminated when the convergence criterion of the l_2 norm of the density errors being less than 1×10^{-6} is satisfied. The computed boundary layer velocity profiles at several x stations are plotted in Fig. 2. It can be seen that all velocity profiles merge into a single curve, and they agree excellently with the Blasius solution.

Case 3: Conical nozzle flow. Consider the internal flow in a conical nozzle studied by Back et al. (1965). The dimensionless nozzle length is 7 based on the radius (r_t) of throat chosen as the characteristic length. The nozzle geometry and the grid used are shown in Fig. 3a. On the nozzle wall, the boundary condition is the no-slip condition. At the inflow boundary, the Riemann invariants are applied to obtain the flow quantities there. On the symmetry axis, a second-order extrapolation from Harten and Osher (1987) is applied. At the nozzle exit, the flow is mainly supersonic and the flow quantities at the exit are extrapolated from the interior points. Chang et al. (1988) have shown that the extrapolation condition is normally able to produce reasonable results for viscous supersonic nozzle flows. An isentropic solution is chosen to be an initial guess. Numerical iteration is terminated when the convergence criterion of the l_2 norm of the density errors being less than 1×10^{-6} is satisfied. The inflow total pressure and total temperature were 17.3 bar and 833.3 K, respectively. The Reynolds number was chosen to be 1.8×10^6 based on the experimental data from Back et al.

The computed pressure distributions along the nozzle walls and the symmetry axis are shown in Figs. 3b,c and compared with the experimental data from Back et al. It can be seen that the flow is accelerated from subsonic to supersonic through the throat. Moreover, the sonic point does not occur exactly at the throat ($x = 0$), but, at $x = 0.2$. At the exit, the flow Mach number is about 2.9. The numerical result agree well with the experimental measurements.

Case 4: A 2D shock wave focusing problem. Consider a plane shock wave which is incident on a plane, concave, parabolic reflector with a focal length (f) of 12.5 mm. The aperture width (H) is 65 mm. We already have some experimental data obtained from our own shock tube facility. The experimental setup was described in the dissertation by Wu (1997). The incident shock Mach number is chosen to be 1.2 and 1.85. For the $M_S = 1.2$ case, the initial pressure ahead of the incident shock was set to be about 10^5 Pa (750 torr). The Reynolds number is 361500. For the $M_S = 1.85$ case, the pressure ahead of the incident shock wave was about 1.33×10^4 Pa (100 torr). The Reynolds number for $M_S = 1.85$ is 81760. Four grids 100 × 100 (grid 1), 150 × 150 (grid 2), 200 × 200 (grid 3), 250 × 250 (grid 4), were used to study the effect of the grid number on the numerical solution. A 200 × 200 grid with a subplot for the grid points near the reflector center is shown in Fig. 4. Figure 5 shows the variation of the maximum pressure ratio with the grid number. The maximum pressure ratio is defined as the maximum pressure normalized by the pressure (P_2) behind the incident shock wave. It is found that the variation in the maximum pressure ratios is 7.1% when grid 1 is changed to grid 2, 3.9% for changing grid 2 to grid 3, and 1.5% for changing grid 3 to grid 4. Since the improvement on the maximum pressure ratio is small for a grid finer than grid 3, grid 3 is used, and will be used for the later study of the axisymmetric case.

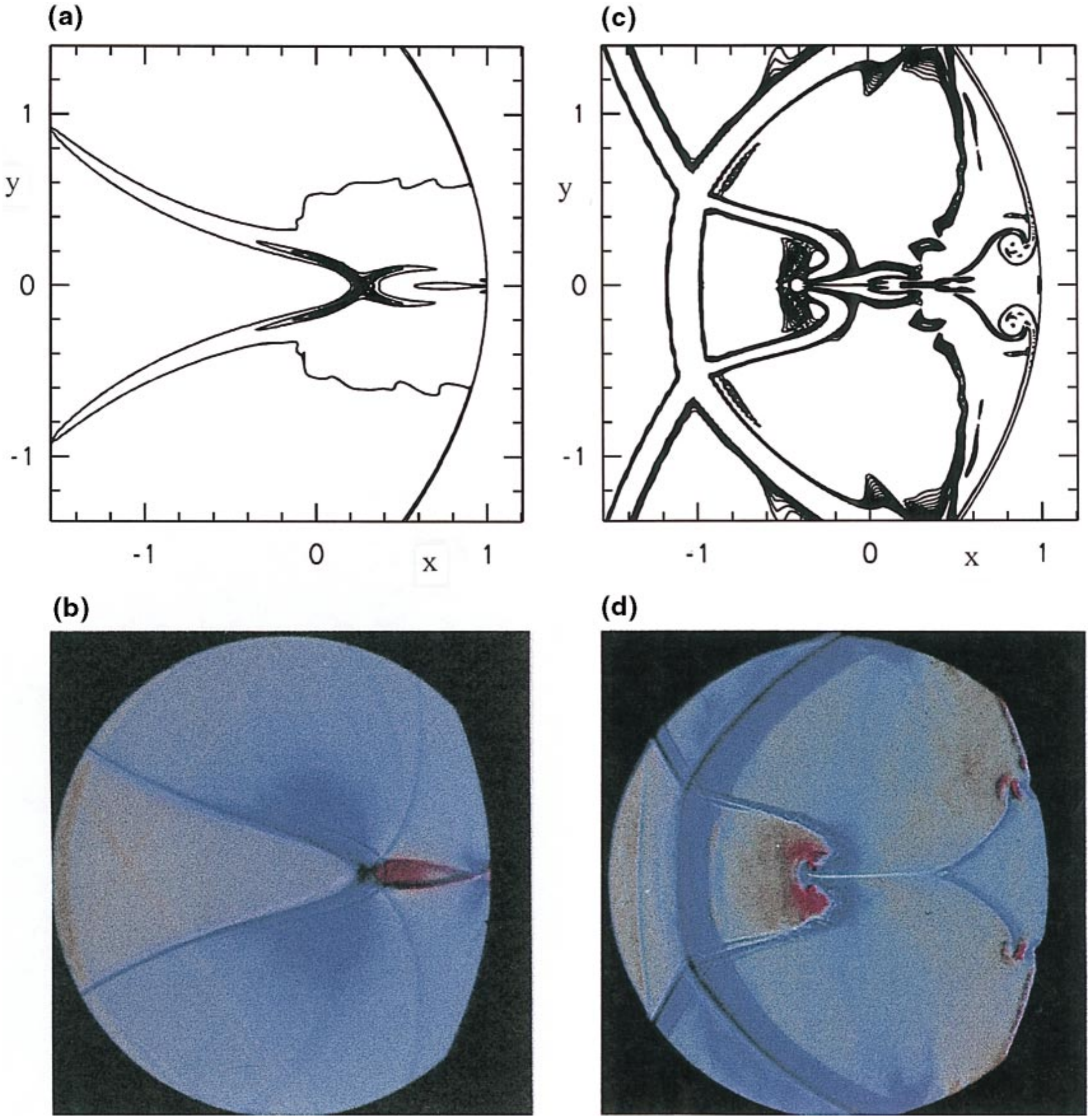

Fig. 6. a, c Computer schlieren graphs. **b, d** Color schlieren photographs for the 2D parabolic reflector. **a, b** $t = 0.5$, $M_S = 1.2$; **c, d** $t = 1.559$, $M_S = 1.85$

Figure 6 shows the comparison of the computer schlieren graphs with the color schlieren photographs after shock wave focusing for $M_S = 1.2$ and 1.85. One can see that the computed reflected shock wave patterns agree well with those obtained from the experiments in both cases. Unfortunately the slipline could not be resolved by the present solver. In the case of a weaker incident shock wave with $M_S = 1.2$, no visible vortex is found, as seen in Fig. 6a,b. But, for a stronger shock wave with $M_S = 1.85$, vortices are generated after shock wave focusing, which can be clearly seen from Fig. 6c and from the red color regions in Fig. 6d. The vortices are generated at the ends of the sliplines.

We also compared the computed maximum pressure distributions along the symmetry axis for $M_S = 1.2$ and 1.85 with the experimental data (Wu, 1997). A reasonable agreement is obtained.

3.2 Results for the axisymmetric reflector

Values of parameters. The flow field of shock wave focusing over a concave reflector is mainly influenced by the two parameters: the reflector depth and the incident shock Mach number. The reflector depth is defined by the ratio of the aperture length (H) to the geometrical focal length (f). The reflector shape and the grid used are shown in Fig. 4a,b. Based on our experimental reflector model in test case 4, two different shapes of the reflector are chosen: $H/f = 5.2$ (model 1), and $H/f = 8.5$ (model 2). The aperture length is fixed to be $H = 65$ mm. So the Model 1 reflector has a focal length of $f = 12.5$ mm and the model 2 reflector has $f = 7.69$ mm. For convenience, the reflector focus is chosen to be the coordinate origin. Thus we have dimensional coordinates $x = (\bar{x} - f)/f, y = \bar{y}/f$. As in test case 4, the incident shock Mach number (M_S) is chosen to

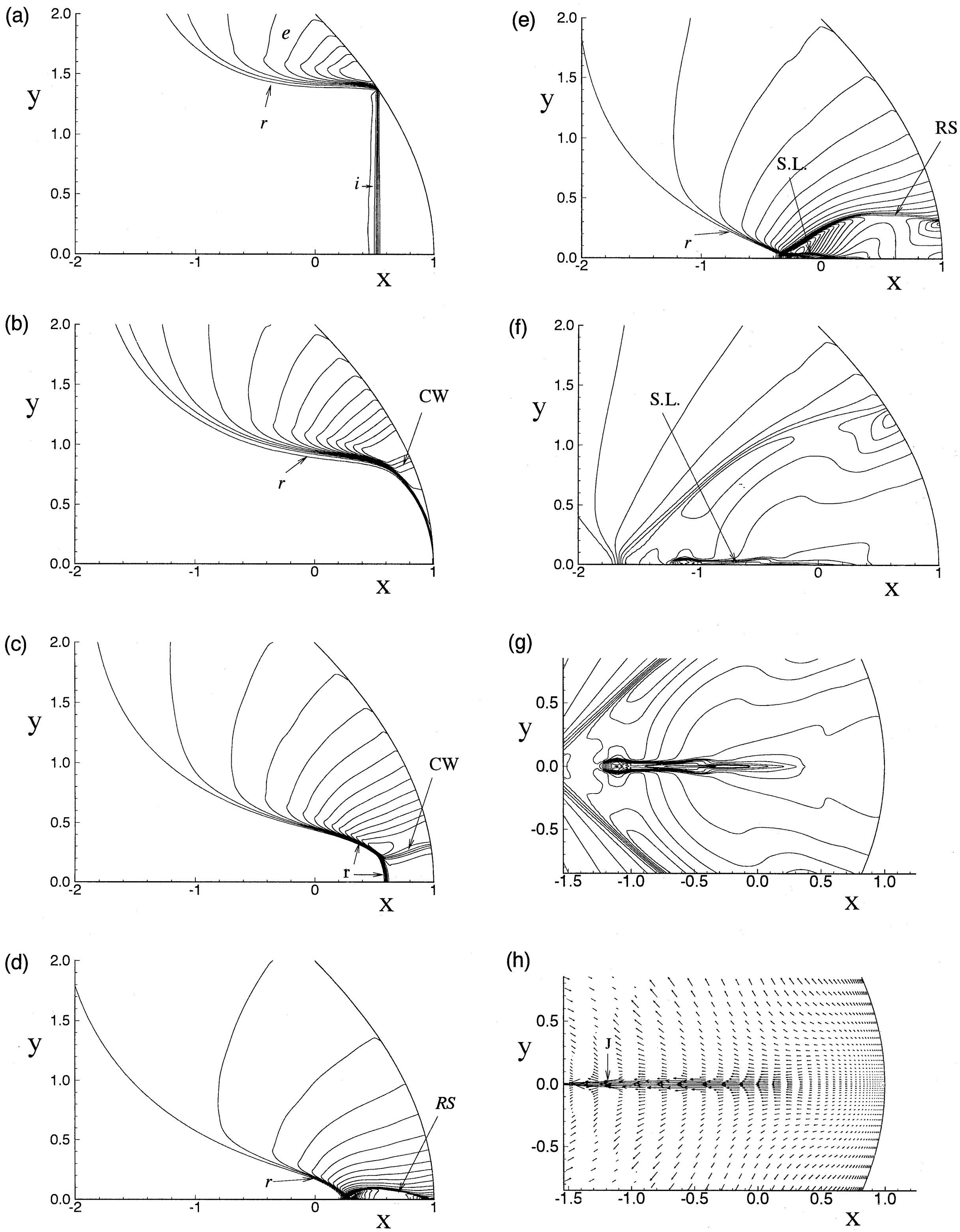

Fig. 7a–h. The isopycnic fields at different instants for the axisymmetric reflector of model 1; $M_S = 1.2$. **a** $t = -0.286$; **b** $t = 0$; **c** $t = 0.285$; **d** $t = 0.429$; **e** $t = 0.571$; **f** $t = 1.036$; **g** locally enlarged graph of isopycnics at $t = 1.036$; **h** its corresponding velocity field

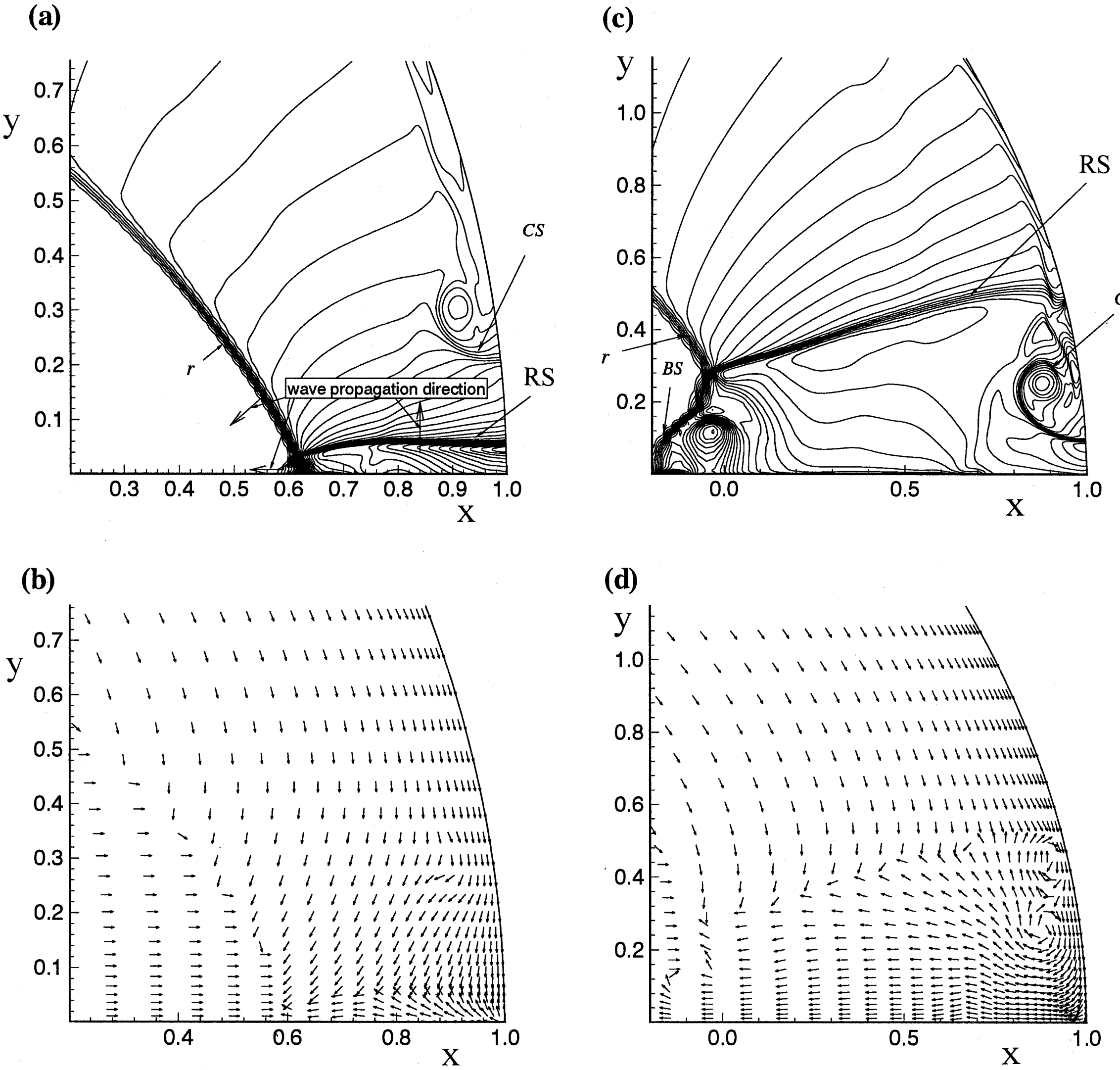

Fig. 8. **a, c** Isopycnics and **b, d** velocity fields for the axisymmetric reflector of model 1, $M_S = 1.85$. **a, b** $t = 0.269$; **c, d** $t = 0.527$

be $M_S = 1.2$ and 1.85. Thus the flow parameter values are the same as those in the 2D shock wave focusing problem.

The dimensionless time (t) is reset to be zero ($t = 0$) when the incident shock wave is totally reflected. So the flow corresponds to a negative instant before the shock wave is totally reflected, and positive for the flow after total wave reflection.

Analysis of flow patterns. Case 1: The model 1 reflector with $M_S = 1.2$. Figure 7 shows the isopycnic fields at different (dimensionless) instants. When $t < 0$, the type of shock wave reflection is of regular reflection. From Fig. 7a, one can clearly see the incident shock wave (i), the reflected shock wave (r) and the expansion wave (e) before the incident shock is totally reflected. When $t = 0$, the incident shock wave completed a total reflection. After that, the reflected shock wave became a converging, concave wave. In addition, compression waves indicated by CW are developed along the reflector surface, as shown in Fig. 7b. These waves are propagating toward the reflector center, as shown in Fig. 7c, and will develop into a ring-shaped shock wave (RS). At this instant the concave reflected shock wave is also converging toward the symmetry axis. The converging process continues as time advances, and the pressure and the temperature behind the reflected shock wave are increasing. As $t = 0.429$, the ring-shaped shock comes out again after a merging process, as shown in Fig. 7d. The converging reflected shock wave starts to focus, later resulting in a maximum pressure and a maximum temperature. Table 1 shows the computed maximum pressures and maximum temperatures and their locations at different incident Mach numbers. Note that the maximum pressure and maximum temperature have been normalized by the flow condition behind the incident shock wave. The maximum pressure and temperature ratios are approximately 20 and 2.8, respectively, which are greater than those for the two-dimensional case. The maximum pressure occurs at $x = 0.44$, and the maximum temperature at $x = 0.30$. The reason for this difference is not clear yet, and it needs further investigation by using a

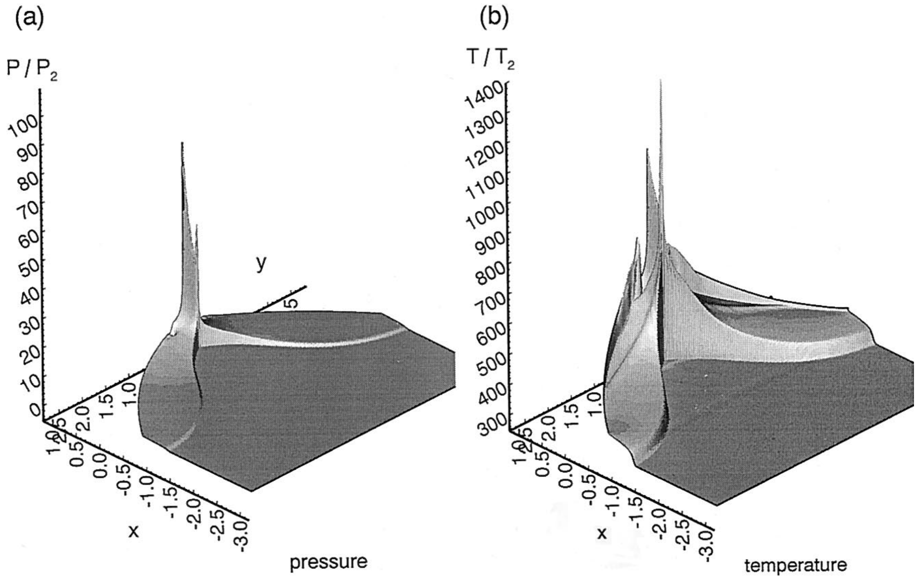

Fig. 9. **a** Pressure and **b** temperature ratio distributions for the model 1 reflector; $M_S = 1.85$, $t = -0.247$

non-equilibrium model. Moreover, the gasdynamic focus is found to be different from the geometrical focus, the coordinate origin. When $t = 0.571$, after shock wave focusing, the pattern of the reflected shock wave is of simple Mach reflection. So a ring-shaped slipline (SL) is developed, as shown in Fig. 7e. At this instant, the maximum pressure and maximum temperature are decreased compared to those at the focusing instant. Later on, the ring-shaped slipline merges on the symmetry axis, as shown in Fig. 7f,g. Because of the slipline formation, a local jet flow (J) is developed, as shown in Fig. 7h.

Case 2: Model 1 reflector with $M_S = 1.85$. The flow field is more complicated than those in case 1. Figure 8a,c shows the flow fields before and after the ring-shaped shock (RS) crosses a complicated structure indicated by CS. By observing the color schlieren photograph in the corresponding 2D problem, we thought that the complicated structure was developed at the end of the slipline emitted from the triple point. From Fig. 8b, one can see that there is no visible vortical flow near the reflector before the wave passes the complicated structure. After the wave passes the complicated structure, vortices are generated, as shown in Fig. 8d. Table 1 compares the computed results for $M_S = 1.2$ and $M_S = 1.85$. One can see that the maximum pressure and the maximum temperature occur at different locations. For $M_S = 1.85$, the maximum pressure occurs at the reflector center, $x = 1$, which is different from the gasdynamic focus ($x = 0.44$) in the previous case. This is due to the contribution of the ring-shaped shock wave merging at the reflector center. But, the maximum temperature occurs at $x = 0.54$. Figure 9a,b shows the pressure and temperature ratio fields at $t = 0.247$. There are two pressure peaks. The front pressure peak is lower than the back one that occurs at the reflector center. There are four temperature peaks – two on the symmetry axis, one on each side of the symmetry axis. Both the front pressure and temperature peaks result from shock wave focusing. The front temperature peak is highest among the four peaks. For $M_S = 1.85$, a stronger jet flow was generated on the symmetry axis than that occurring in case 1, and it also induced vortices behind the reflected shock wave. The generation of vortices is due to the non-zero pressure and non-zero density gradients behind the reflected shock wave.

Case 3: Model 2 reflector with $M_S = 1.2$. Since the model 2 reflector ($H/f = 8.5$) is deeper than the model 1 reflector ($H/f = 5.2$), the reflected shock wave (r) is more curved so that parts of the reflected wave cross each other after total wave reflection. A closed-loop shock wave is developed, which occupies a small region before shock wave focusing. Figure 10 shows the pressure and temperature ratio fields at $t = 0.111$ and $t = 0.114$. When $t = 0.111$, before the RS shock wave crosses the reflector center, as mentioned in case 1, there are two pressure peaks and two temperature peaks. The highest pressure peak and the highest temperature peak occur near the focal point. When $t = 0.114$ after the RS shock crosses the reflector center, the highest pressure peak occurs at $x = 1$ and the highest temperature peak occurs at $x = 0.396$. In this case, there is almost no vortical flow developed near the reflector.

Case 4: Model 2 reflector with $M_S = 1.85$. In this case, the type of shock wave reflection from the reflector for $t < 0$ was found to be of simple Mach reflection, as shown in Fig. 11a,b. When $t = 0$, an implosion phenomenon happened, as shown in Fig. 11c. The implosion phenomenon results from the merging of the incident shock wave and the Mach stem at the reflector center. As mentioned by Milton (1989), an implosion is a type of maximization of energy concentration at a single point. The maximum pressure and temperature ratios were found to be as high as 1285 and 13, respectively. In the study of a shock wave

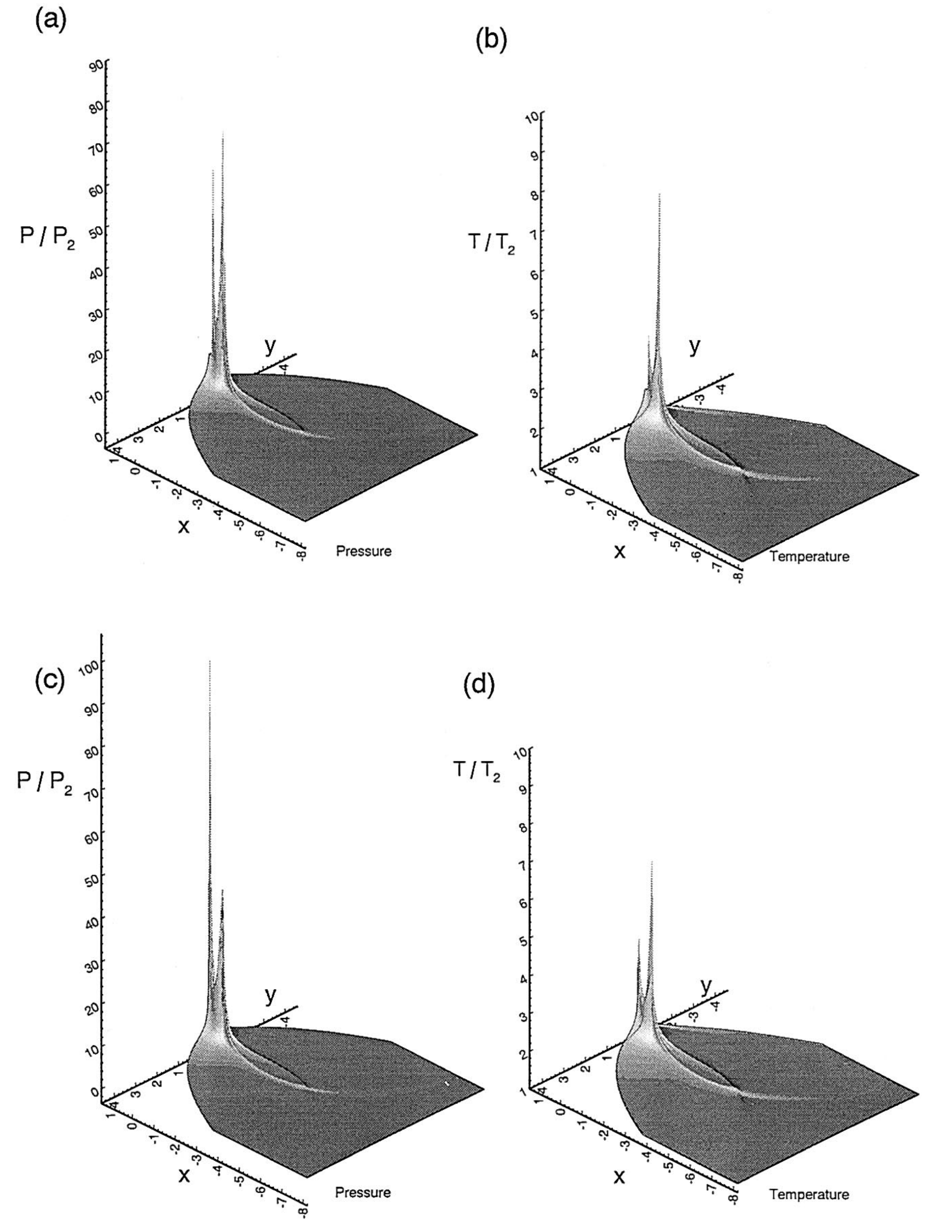

Fig. 10a–d. The fields of the (**a, c**) pressure and (**b, d**) temperature ratios for the axisymmetric reflector of model 2; $M_S = 1.2$. **a, b** $t = 0.111$; **c, d** $t = 0.114$

Table 1. The computed result for the axisymmetric reflector of model 1 at two different incident Mach numbers

M_S	$P_{\max}/P_2(\mathrm{Axi} : 2\mathrm{D})^{\dagger}$	$T_{\max}/T_2(\mathrm{Axi} : 2\mathrm{D})$	Location of max. pressure (x)	Location of max. temperature (x)
1.2	19.7 : 3.34	2.76 : 1.45	0.44	0.30
1.85	24.8 : 6.88	3.61 : 1.93	1.0	0.54

† (Axi : 2D) means that the maximum pressure ratio for the axisymmetric case versus that for the corresponding two-dimensional case.
The subscript 2 denotes the flow condition ahead of the incident shock wave

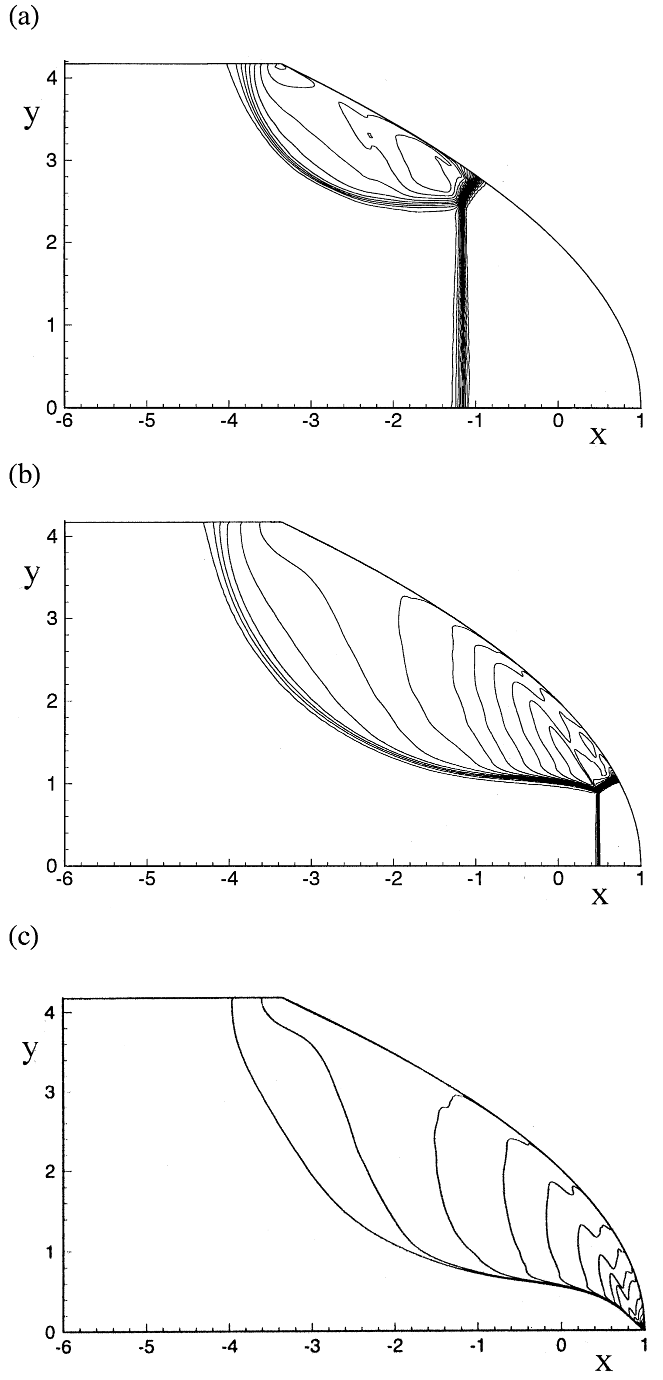

Fig. 11a–c. The isopycnic fields for the axisymmetric reflector of model 2, $M_S = 1.85$. **a** $t = -0.117$; **b** $t = -0.012$; **c** $t = 0$

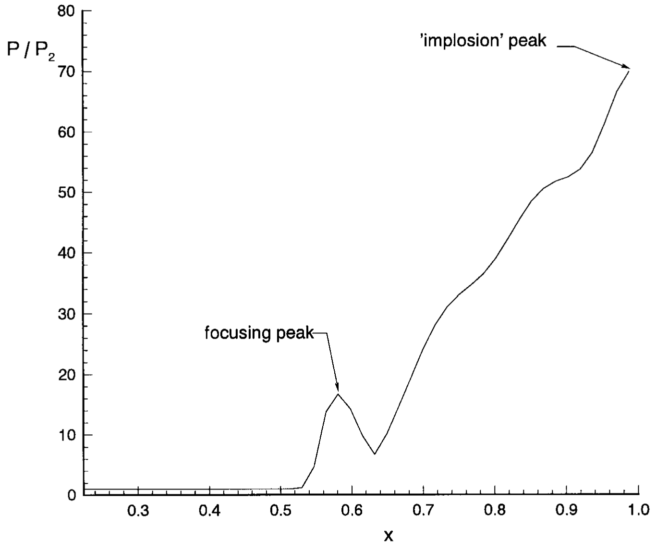

Fig. 12. Pressure ratio distribution along the symmetry axis for the axisymmetric reflector of model 2 at $t = 0.03$, $M_S = 1.85$

focusing problem, Kishige et al. (1991) confirmed the existence of a high temperature. After implosion, the reflected shock wave started to focus, resulting in a second pressure peak as shown in Fig. 12. The second pressure peak is lower than the maximum pressure at the reflector center. The Reynolds number is also investigated by increasing the value of the Reynolds number from 81760 to 1.2×10^5. It was found that the effect of the Reynolds number on the pressure and temperature magnifications is almost negligible; the inviscid flow dominates the shock wave focusing flow problem.

Comparison of axisymmetric and 2D shock wave focusing. When an incident shock wave propagates in a contracting channel, the shock wave becomes stronger because of a compression effect. Similarly, for an incident shock with partial reflection from the paraboloidal reflector, the incident shock becomes stronger. After total wave reflection, the reflected shock wave, coming from all directions, is focused at a point. Thus the pressure enhancement is much greater than that for the two-dimensional case. On the other hand, since an implosion might happen for the axisymmetric case, the enhanced pressure at the reflector center could be higher than the pressure at gasdynamic focus. However, the temperature did not behave like that. Tables 1 and 2 tabulate the computational results for the reflectors of models 1 and 2. For the model 1 reflector, from Table 1 we can see that the pressure and the temperature magnifications in the axisymmetric case are 19.7 and 2.8 for $M_S = 1.2$, and are 24.8 and 6.9 for $M_S = 1.85$, respectively, which are much greater than those for the two-dimensional case.

For the model 2 reflector at $M_S \geq 1.65$, the incident shock wave and the Mach stem arrived at the reflector center simultaneously and merged there, resulting in an implosion phenomenon as indicated in Table 2. Thus the maximum pressure and the maximum temperature occurred at $x = 1$, the reflector center. The pressure magnification was found to be much greater than that in the two-dimensional case, as shown in Table 2. However, the temperature magnification is not as large as the pressure magnification. From Tables 1 and 2, it is concluded that the pressure and temperature magnifications are affected by the two factors: the reflector depth and the incident shock Mach number. The effects of the two factors on the pressure magnification are more significant than the tem-

Table 2. The computed result for the axisymmetric reflector of model 2 at four different incident Mach numbers

M_S	$P_{\max}/P_2(\mathrm{Axi} : 2\mathrm{D})^{\dagger}$	$T_{\max}/T_2(\mathrm{Axi} : 2\mathrm{D})$	Location of max. pressure (x)	Location of max. temperature (x)
1.2	90 : 4.6	6.90 : 1.62	1.0	0.40
1.65*	470 : 9.6	7.06 : 2.23	1.0	1.0
1.85*	1139 : 11.5	12.8 : 2.31	1.0	1.0
2.00*	1285 : 12.4	13.0 : 2.39	1.0	1.0

* means that implosion happened

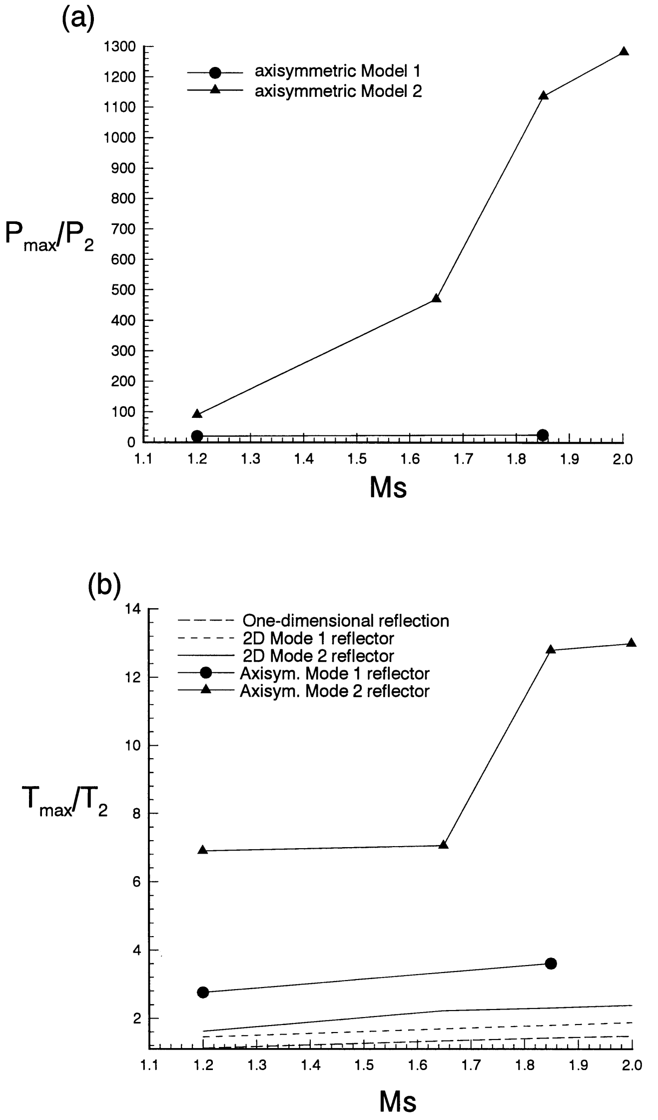

Fig. 13a,b. The variations of the maximum pressure **a** and maximum temperature **b** ratios for different incident shock Mach numbers

perature magnification. Moreover, the pressure and temperature magnifications in the axisymmetry case is much greater than those in the 2D case.

Figure 13 shows the variations of the pressure and temperature magnifications for different incident shock Mach numbers and different-depth reflectors. For the deeper reflector (model 2), the pressure magnification is increased exponentially with the incident shock Mach number. For the model 1 reflector, the pressure magnification grows much slower than that for the model 2 reflector, as shown in Fig. 13a. Note that for the deeper reflector the temperature magnification is increased exponentially with the incident shock Mach number up to 1.85 and then increased gradually with M_S for $M_S > 1.85$, as shown in Fig 13b. From Fig. 13b, we also found that the temperature magnifications for the 2D reflector of model 2 and for the axisymmetric reflector of model 1 are increased linearly with the incident shock Mach number. The one-dimensional result of shock wave reflection from a plain wall was included for comparison, as indicated by the bottom dashed line. The dashed line next to the bottom line represents the result for the case of a two-dimensional model 1 reflector. The solid line without symbols represents the result for the case of a two-dimensional model 2 reflector.

4 Conclusion

Numerical investigation of shock wave focusing over axisymmetric paraboloidal reflectors with different depths at various incident shock Mach numbers has been carried out. A robust numerical solver with a simple equilibrium model for real-gas effects was developed by an improved TVD scheme. An inner iteration for enhancing stability and accuracy was also included. The solver was verified to be reasonably accurate on the test problems. For the paraboloidal reflector, it was found that the pressure and temperature magnifications are much greater than those for the two-dimensional case. Moreover, an implosion phenomenon can occur, depending on the incident shock Mach number. For the deeper axisymmetric reflector of model 2, the implosion occurred at the reflector center and at a lower incident shock Mach number, compared to the shallower reflector of model 1. Also, the implosion can cause extremely large pressure magnification. Using the simple equilibrium model for real-gas effects, it was found that the location where a maximum temperature occurred can be different from the gasdynamic focus. The reason for this difference needs further investigation using a non-equilibrium model. Vortical flows caused by axisymmetric shock wave focusing and their formation mechanism were explored. It was found that the vortices near the reflector are caused by a ring-shaped shock/slipline interaction. Due to the slipline formation at the symmetry axis, a jet flow could be induced. The jet flow resulted in vortices near the symmetry axis.

Acknowledgements. The support for this study under the National Science Council contracts, NSC 86-2212-E-006-061 and NSC 86-2622-E-006-004, is gratefully acknowledged. We are also indebted to the reviewers' valuable comments and suggestions.

References

Apazidis N (1994) Focusing of weak shock waves in confined axisymmetric chambers. Shock Waves, 3:201-212

Back LH, Massier PF, Gier HL (1965) Comparison of measured and predicted flows through conical supersonic nozzle with emphasis on the transonic region. AIAA J, 3:1606-1613

Ben-Dor G (1992) Shock wave reflection phenomena. Springer-Verlag New York

Chang CL, Kronzon Y, Merkle, CL (1988) Time-iteration solutions of viscous supersonic nozzle flows. AIAA J, 26:1208-1215

Grossman B, Walters RW (1989) Analysis of flux split algorithm for Euler equations with real gases. AIAA J, 7:524-531

Harten A and Osher S (1987) Uniformly high-order accurate non-oscillatory schemes. SIAM, J Num Anal, 24:279-309

Holl R, Higashino F, Sakamoto I (1991) Shock dynamics method for focusing of reflected blast waves. Proc 18th Symp Shock Waves, 1:337-340

Izumi K, Aso S, Nishida M (1991) Experimental and computational studies on focusing processes of shock waves reflected from parabolic reflectors. Shock Waves, 4:217-224

Kishige H, Teshima K, Nishida M (1991) Focusing of shock waves reflected from an axisymmetric parabolic wall. Proc 18th Symp Shock Waves, 1:341-345

Liang SM, Tsai CJ, Wu LN (1996) Efficient, robust second-order total variation diminishing scheme. AIAA J, 34:193-195

Milton BE (1989) The focusing of shock waves in two dimensional and axisymmetric ducts. Takayama K (ed), Int Workshop on Shock Wave Focusing, Institute of Fluid Science, Tohuku University, Japan, 155-191

Roe PL (1981) Approximate Riemann solvers, parameter vectors, and difference schemes. J Comp Phys, 43:357-372

Srinivasan S, Tannehill J C, Weilmuenster KJ (1987) Simplified curve fits for the thermodynamic properties of equilibrium air. NASA RP-1181

Takayama K, Ben-Dor G (1985) Reflection and diffraction of shock waves over a circular concave wall. Report No. 378, Institute of High Speed Mechanics, Tohoku University, Japan

Yee HC, Harten A (1987) Implicit TVD schemes for hyperbolic conservation Laws in curvilinear coordinates. AIAA J, 25:266-27

Wu RN (1997) Experimental and numerical studies on vortical flows induced by shock wave focusing over parabolic reflectors. Ph. D. dissertation, Institute of Aeronautics and Astronautics, National Cheng Kung University, Taiwan, ROC